Progressive Band Processing of Constrained Energy Minimization for Subpixel Detection

Chein-I Chang, *Fellow, IEEE*, Robert C. Schultz, Marissa C. Hobbs, Shih-Yu Chen, Yulei Wang, and Chunhong Liu

***Abstract*—Constrained energy minimization (CEM) has been widely used for subpixel detection. It takes advantage of inverting the global sample correlation matrix $\mathbf{R}$ to suppress background so as to enhance detection of targets of interest. This paper presents a progressive band processing of CEM (PBP-CEM) which can perform CEM for target detection progressively band by band according to band sequential format. In doing so, a new concept, called causal band correlation matrix (CBCM), is introduced to replace the global sample correlation matrix $\mathbf{R}$. It is a global correlation matrix formed by only those bands that were already visited up to the band currently being processed while excluding bands yet to be visited in the future. The proposed PBP-CEM allows CEM to be processed whenever bands are available, without waiting for completing band collection. With such an advantage, CEM has potential in data transmission and communication, specifically in satellite data processing.**

***Index Terms*—Causal band correlation matrix (CBCM), causal CEM (C-CEM), constrained energy minimization (CEM), progressive band processing of CEM (PBP-CEM), real-time CEM (RT-CEM), recursive causal CEM (RC-CEM).**

I. Introduction

SUBPIXEL detection is generally referred to as detection of a material substance of interest which has its spatial presence extent within a single pixel. Specifically, when the target size is smaller than the pixel size, it is then called a subpixel target. There are two major cases which result in a subpixel issue. One is insufficient spatial resolution. As a result, many material substances may partially occupy a single pixel. This is particularly true for multispectral images which are generally acquired by tens of discrete wavelengths with spatial resolution ranging from 20 to 30 m. Under such circumstance, material substances are mixed all together in a single pixel and result in a mixed pixel. As a consequence, it requires subpixel detection to identify target substances involved with such mixing. The second is a result of high spectral resolution resulting from hyperspectral imaging sensors using hundreds of contiguous wavelengths where a target substance embedded in a single pixel can be uncovered as a subpixel target. This is especially important in hyperspectral data exploitation because subpixel targets provide crucial information for image analysts. In either case, subpixel detection plays a key role in image interpretation.

Despite that many target detection algorithms have been proposed in the past [1]–[7] the constrained energy minimization (CEM) developed in [8] has shown great success in subpixel detection, where its idea was originally derived from [9] and has been studied extensively in [10] and [11]. The CEM assumes that there is a desired signature specified by $\mathbf{d}$. It then uses this designated signature to custom-design a finite impulse response (FIR) filter to pass data samples matched by $\mathbf{d}$ through a constraint while minimizing the least squares error caused by unmatched data samples. The major strength of CEM is no prior knowledge required for data processing other than the desired signature $\mathbf{d}$. This advantage is very significant since so many signal sources cannot be either identified or inspected visually due to the fact that these substances are very likely to be extracted unknowingly by a sensor. Finding these signal sources is either impossible or extremely difficult. Using the specified signature $\mathbf{d}$ allows users to extract targets of interest without knowing the background *a priori*. As a matter of fact, CEM takes advantage of the sample correlation matrix $\mathbf{R}$ to perform background suppression via inverting $\mathbf{R}$ before it extracts the desired signature $\mathbf{d}$. With background suppression by $\mathbf{R}^{-1}$ followed by a matched filter, using the signature $\mathbf{d}$ as its matched signal CEM not only enhances its signal detectability but also performs very effectively. Interestingly, using the inversion of $\mathbf{R}$ has the same effect as that resulting from orthogonal subspace projection (OSP) complement used by linear spectral mixture analysis as discussed in [12]. Recently, a progressive CEM has been further proposed in [13] by adapting $\mathbf{R}$ to incoming data samples to further make CEM a real-time processing algorithm as data collection is carried out sample by sample according to the band-interleaved-by-sample/band-interleaved-by-pixel (BIS/BIP) format [14]. This paper takes a rather different approach by adapting both $\mathbf{R}$ and $\mathbf{d}$ to varying

Manuscript received September 8, 2013; revised June 7, 2014; accepted July 14, 2014. The work of C. Liu was supported by the Youth National Natural Science Foundation of China (61201415). *(Corresponding author: Chunhong Liu.)*

C.-I Chang is with the Remote Sensing Signal and Image Processing Laboratory, Department of Computer Science and Electrical Engineering, University of Maryland, Baltimore County, Baltimore, MD 21250 USA, with the Department of Electrical Engineering, National Chung Hsing University, Taichung 402, Taiwan, and also with the Department of Computer Science and Information Engineering, Providence University, Taichung 43301, Taiwan (e-mail: cchang@umbc.edu).

R. C. Schultz and M. C. Hobbs are with the Remote Sensing Signal and Image Processing Laboratory, Department of Computer Science and Electrical Engineering, University of Maryland, Baltimore County, Baltimore, MD 21250 USA.

S.-Y. Chen is with the Department of Computer Science and Information Engineering, National Yulin University of Science and Technology, Yulin 64002, Taiwan (e-mail: koberan3@gmail.com).

Y. Wang is with the Information and Communication Engineering College, Harbin Engineering University, Harbin 150001, China (e-mail: wangyulei.heu@gmail.com).

C. Liu is with the Information and Communication Engineering College, China Agriculture University, Beijing 100083, China (e-mail: 31314209@qq.com).

Color versions of one or more of the figures in this paper are available online at http://ieeexplore.ieee.org.

Digital Object Identifier 10.1109/TGRS.2014.2346479

bands instead of varying data samples. It is called progressive band processing of CEM (PBP-CEM), which implements CEM progressively band by band as each new band is received. This type of data processing is derived from the need of band sequential (BSQ) format [14], where remotely sensed images are acquired and processed band by band.

The proposed PBP-CEM is quite different from traditional band selection (BS) in several aspects. First of all, BS generally requires prior knowledge about the number of bands n_{BS} to be selected, but PBP-CEM does not. Specifically, it can process CEM whenever bands are available. Second, to avoid repeatedly solving BS optimization problems as the value of n_{BS} changes, band prioritization (BP) is developed for BS to rank all bands according to the significance of their contained information [15], [16]. PBP-CEM does not need BP either since bands can come in any order and PBP-CEM processes CEM whenever a new band is acquired. Third, to make BS more effective, band decorrelation is included to remove interband redundancy so that highly correlated bands will not be selected. For PBP-CEM, there is no need for band decorrelation. It simply uses up all of the bands available at the time it is processed.

In order to process PBP-CEM, a new concept must be introduced, to be called causal band correlation matrix (CBCM), which varies band by band. It is a sample correlation matrix formed by all bands that are already visited and processed up to the currently being processed band. For example, assume that $\mathbf{B}_l$ is the current band to be processed, and $\{\mathbf{B}_j\}_{j=1}^{l-1}$ are those bands that are previously processed. The CBCM is a sample correlation matrix formed by all data sample vectors provided by $\{\mathbf{B}_j\}_{j=1}^{l}$ but not data sample vectors in any band $\{\mathbf{B}_j\}_{j=l+1}^{L}$ yet to be visited in the future, where L is the total number of bands. Such causality is derived from the causal Wiener filtering in [17], where only data samples up to the currently being processed sample can be used to process a Wiener filter. By virtue of the CBCM, PBP-CEM performs a progressive process of CEM one band at a time in a band-causal manner. In other words, band-causal processing can be defined as data processing which uses only bands already collected but not those bands yet to be received in the future. Since CBCM must be recalculated every time a new band is received, its computational complexity is exceedingly high. In a similar manner that a Kalman filter is derived from a causal Wiener filter in [17], a novel contribution made by this paper is to derive a recursive innovations information update equation for PBP-CEM to calculate CBCM recursively, where only a new band information is required for updating. This recursive equation is a key to making PBP-CEM possible to be implemented in real time in the sense of band processing.

II. CEM

The idea of CEM can be traced back to linearly constrained minimum variance originally proposed by Frost, III, for adaptive beamforming [18]. Suppose that a hyperspectral image is acquired by BIS/BIP and represented by a collection of image pixel vectors, denoted by $\{\mathbf{r}_1, \mathbf{r}_2, \ldots, \mathbf{r}_N\}$, where $\mathbf{r}_i = (r_{i1}, r_{i2}, \ldots, r_{iL})^T$ for $1 \leq i \leq N$ is an L-dimensional pixel vector, N is the total number of pixels in the image, and L is the total number of spectral channels. Further assume that $\mathbf{d} = (d_1, d_2, \ldots, d_L)^T$ is specified by a desired signature of interest to be used for target detection. The goal is to design a target detector finding data samples specified by the desired target signal $\mathbf{d}$ via a FIR linear filter with L filter coefficients $\{w_1, w_2, \ldots, w_L\}$, denoted by an L-dimensional vector $\mathbf{w} = (w_1, w_2, \ldots, w_L)^T$ which minimizes the filter output energy subject to the constraint $\mathbf{d}^T\mathbf{w} = \mathbf{w}^T\mathbf{d} = 1$. More specifically, let y_i denote the output of the designed FIR filter resulting from the input $\mathbf{r}_i$. Then, y_i can be expressed by

$$y_i = \sum_{l=1}^{L} w_l r_{il} = (\mathbf{w})^T \mathbf{r}_i = \mathbf{r}_i^T \mathbf{w} \tag{1}$$

and the average energy of the filter output is given by

$$\begin{aligned}\left(\frac{1}{N}\right)\sum_{i=1}^{N} y_i^2 &= \left(\frac{1}{N}\right)\sum_{i=1}^{N}\left(\mathbf{r}_i^T\mathbf{w}\right)^2 \\ &= \mathbf{w}^T\left[\left(\frac{1}{N}\right)\sum_{i=1}^{N}\mathbf{r}_i\mathbf{r}_i^T\right]\mathbf{w} \\ &= \mathbf{w}^T\mathbf{R}\mathbf{w}\end{aligned} \tag{2}$$

where $\mathbf{R} = (1/N)[\sum_{i=1}^{N}\mathbf{r}_i\mathbf{r}_i^T]$ is the autocorrelation sample matrix of the image. CEM is developed to solve the following linearly constrained optimization problem:

$$\min_{\mathbf{w}}\{\mathbf{w}^T\mathbf{R}\mathbf{w}\} \text{ subject to } \mathbf{d}^T\mathbf{w} = \mathbf{w}^T\mathbf{d} = 1. \tag{3}$$

The optimal solution to (3) is given by

$$\mathbf{w}^{\mathrm{CEM}} = \frac{\mathbf{R}^{-1}\mathbf{d}}{\mathbf{d}^T\mathbf{R}^{-1}\mathbf{d}}. \tag{4}$$

With the optimal weight $\mathbf{w}^{\mathrm{CEM}}$ specified by (4), a filter called CEM, denoted by $\delta^{\mathrm{CEM}}(\mathbf{r})$, was derived in Harsanyi [9] as

$$\delta^{\mathrm{CEM}}(\mathbf{r}) = (\mathbf{w}^{\mathrm{CEM}})^T\mathbf{r} = \left(\frac{\mathbf{R}^{-1}\mathbf{d}}{\mathbf{d}^T\mathbf{R}^{-1}\mathbf{d}}\right)^T\mathbf{r} = \frac{\mathbf{d}^T\mathbf{R}^{-1}\mathbf{r}}{\mathbf{d}^T\mathbf{R}^{-1}\mathbf{d}}. \tag{5}$$

III. PBP-CEM

Assume that $\{\mathbf{r}_i\}_{i=1}^{N}$ is a set of all data sample vectors in the lth band. We also let $\mathbf{X}_l = [\mathbf{r}_1\mathbf{r}_2\ldots\mathbf{r}_{N-1}\mathbf{r}_N]$ be the data matrix formed by $\{\mathbf{r}_i\}_{i=1}^{N}$. Let

$$\begin{aligned}\mathbf{X}_l &= [\mathbf{r}_1\mathbf{r}_2\ldots\mathbf{r}_{N-1}\mathbf{r}_N] \\ &= \begin{bmatrix} r_{11} & \cdots & r_{(N-1)1} & r_{N1} \\ \vdots & \ddots & \vdots & \vdots \\ r_{1(l-1)} & \cdots & r_{(N-1)(l-1)} & r_{N(l-1)} \\ r_{1l} & \cdots & r_{(N-1)l} & r_{Nl} \end{bmatrix}\end{aligned}$$

and $\mathbf{X}_l = \left[\begin{smallmatrix}\mathbf{X}_{l-1} \\ \mathbf{x}^T(l)\end{smallmatrix}\right]$, where

$$\mathbf{X}_{l-1} = \begin{bmatrix} r_{11} & \cdots & r_{(N-1)1} & r_{N1} \\ \vdots & \ddots & \vdots & \vdots \\ r_{1(l-2)} & \cdots & r_{(N-1)(l-2)} & r_{N(l-2)} \\ r_{1(l-1)} & \cdots & r_{(N-1)(l-1)} & r_{N(l-1)} \end{bmatrix}$$

$\mathbf{x}(l) = (r_{1l}, r_{2l}, \ldots, r_{Nl})^T$ is an N-dimensional data sample vector formed by the data samples of $\{\mathbf{r}_i\}_{i=1}^N$ in the lth bands. The CBCM up to the lth band $\mathbf{B}_l$ is then defined by $\mathbf{R}_{l\times l} = (1/N)\mathbf{X}_l\mathbf{X}_l^T$, which can be expressed as

$$N\mathbf{R}_{l\times l} = \mathbf{X}_l\mathbf{X}_l^T = \begin{bmatrix} \mathbf{X}_{l-1} \\ \mathbf{x}^T(l) \end{bmatrix} \begin{bmatrix} \mathbf{X}_{l-1}^T & \mathbf{x}(l) \end{bmatrix} = \begin{bmatrix} \mathbf{X}_{l-1}\mathbf{X}_{l-1}^T & \mathbf{X}_{l-1}\mathbf{x}(l) \\ \mathbf{x}^T(l)\mathbf{X}_{l-1}^T & \mathbf{x}^T(l)\mathbf{x}(l) \end{bmatrix}. \tag{6}$$

In order to find a recursive formula of $\mathbf{R}_{l\times l}^{-1}$, we use the following matrix identity (7) derived in [19], which was used to derive the relationship between OSP and least squares solution:

$$[\mathbf{M}^T\mathbf{M}]^{-1} = \begin{bmatrix} \mathbf{U}^T\mathbf{U} & \mathbf{U}^T\mathbf{d} \\ \mathbf{d}^T\mathbf{U} & \mathbf{d}^T\mathbf{d} \end{bmatrix}^{-1} = \begin{bmatrix} (\mathbf{U}^T\mathbf{U})^{-1} + \beta\mathbf{U}^{\#}\mathbf{d}\mathbf{d}^T(\mathbf{U}^{\#})^T & -\beta\mathbf{U}^{\#}\mathbf{d} \\ -\beta\mathbf{d}^T(\mathbf{U}^{\#})^T & \beta \end{bmatrix} \tag{7}$$

where $\beta = \{\mathbf{d}^T[\mathbf{I} - \mathbf{U}(\mathbf{U}^T\mathbf{U})^{-1}\mathbf{U}^T]\mathbf{d}\}^{-1} = \{\mathbf{d}^T[P_{\mathbf{U}}^{\perp}]\mathbf{d}\}^{-1}$ and $\mathbf{U}^{\#} = (\mathbf{U}^T\mathbf{U})^{-1}\mathbf{U}^T$. By setting $\mathbf{U} = \mathbf{X}_{l-1}^T$ and $\mathbf{d} = \mathbf{x}(l)$, we obtain

$$\mathbf{X}_{l-1}^{\#} = \left(\mathbf{X}_{l-1}\mathbf{X}_{l-1}^T\right)^{-1}\mathbf{X}_{l-1}$$
$$\beta = \left\{\mathbf{x}^T(l)\left[\mathbf{I} - \mathbf{X}_{l-1}^T\left[\mathbf{X}_{l-1}\mathbf{X}_{l-1}^T\right]^{-1}\mathbf{X}_l\right]\mathbf{x}(l)\right\}^{-1} = \left(\mathbf{x}^T(l)P_{\mathbf{X}_{l-1}^T}^{\perp}\mathbf{x}(l)\right)^{-1}$$
$$P_{\mathbf{X}_{l-1}^T}^{\perp} = \mathbf{I}_N - \mathbf{X}_{l-1}^T\left(\mathbf{X}_{l-1}\mathbf{X}_{l-1}^T\right)^{-1}\mathbf{X}_{l-1}.$$

Finally, the inverse of $\mathbf{R}_{l\times l}$, $\mathbf{R}_{l\times l}^{-1}$, is derived in (A2) in the Appendix.

By taking advantage of (A3), $\delta^{\text{PBP-CEM}}(\mathbf{r}(l))$ can be updated by $\delta^{\text{PBP-CEM}}(\mathbf{r}(l-1))$ as follows:

$$\delta^{\text{PBP-CEM}}(\mathbf{r}(l)) = \left(\frac{\kappa_l}{\kappa_{l-1}}\right)\delta^{\text{PB-CEM}}(\mathbf{r}(l-1)) + \left(\frac{1}{N}\right)\kappa_l\beta_{l|(l-1)}\left(\mathbf{d}^T(l-1)\boldsymbol{\nu}_{l|(l-1)} - Nd_l\right) \times \left(\boldsymbol{\nu}_{l|(l-1)}^T\mathbf{r}(l-1) - Nr_l\right) \tag{8}$$

where $\mathbf{r}(l)$ is an l-dimensional data sample vector given by $\mathbf{r}(l) = (r_1, r_2, \ldots, r_l)^T$, $\kappa_l = (\mathbf{d}^T(l)\mathbf{R}_{l\times l}^{-1}\mathbf{d}(l))^{-1}$, $\mathbf{v}_{l|(l-1)} = \mathbf{R}_{(l-1)\times(l-1)}^{-1}\mathbf{X}_{l-1}\mathbf{x}(l)$, and $\beta_{l|(l-1)} = \{\mathbf{x}^T(l)[P_{\mathbf{X}_{l-1}^T}^{\perp}]\mathbf{x}(l)\}^{-1}$.

Interestingly, from a statistical signal processing point of view, the CEM specified by (8) actually performs as if it is a Kalman filter [20] with a key difference in that only a measure equation also known as output (5) is needed and there is no need of state equation involved in CEM. More specifically, the abundance fractional amount detected by CEM using l bands $\delta^{\text{PBP-CEM}}(\mathbf{r}(l))$ is initiated by the following: 1) the first band information and then updated recursively through three types of information; 2) the new information from the newly received lth band; 3) the processed information produced by using the first $l-1$ bands which have been already visited, including the abundance fractional amount detected by CEM $\delta^{\text{PBP-CEM}}(\mathbf{r}(l-1))$; and 4) the innovations information provided by the correlation between the lth and $l-1$ bands, each of which is described in detail as follows.

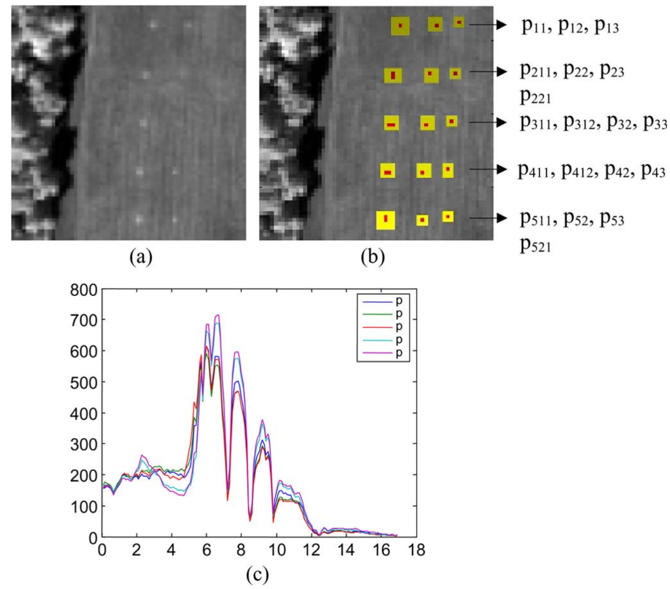

Fig. 1. (a) HYDICE panel scene which contains 15 panels. (b) Ground truth map of spatial locations of the 15 panels. (c) Five panel signatures $\mathbf{p}_1$, $\mathbf{p}_2$, $\mathbf{p}_3$, $\mathbf{p}_4$, and $\mathbf{p}_5$.

1) Initial conditions:

$$\mathbf{d}(1),\ \mathbf{r}(1),\ \mathbf{R}(1) = \mathbf{r}(1)\mathbf{r}^T(1).$$

2) Input information from all data sample vectors: $\{r_{il}\}_{i=1}^N$ in the lth band $\mathbf{B}_l$ to form $\mathbf{x}(l)$ and $\kappa_l = (\mathbf{d}^T(l)\mathbf{R}_{l\times l}^{-1}\mathbf{d}(l))^{-1}$.

3) Available processed information by $(l-1)$ bands: $\mathbf{r}(l-1)$, $\mathbf{R}_{(l-1)\times(l-1)}^{-1}$, $\mathbf{X}_{l-1}$, $\delta^{\text{PBP-CEM}}(\mathbf{r}(l-1))$

$$P_{\mathbf{X}_{l-1}^T}^{\perp} = \mathbf{I}_N - \mathbf{X}_{l-1}^T\left(\mathbf{X}_{l-1}\mathbf{X}_{l-1}^T\right)^{-1}\mathbf{X}_{l-1} = \mathbf{I}_N - N\mathbf{X}_{l-1}^T\mathbf{R}_{(l-1)\times(l-1)}^{-1}\mathbf{X}_{l-1}.$$

4) Innovations information

$$\beta_{l|(l-1)} = \left\{\mathbf{x}^T(l)\left[P_{\mathbf{X}_{l-1}^T}^{\perp}\right]\mathbf{x}(l)\right\}^{-1}$$
$$\boldsymbol{\nu}_{l|(l-1)} = \mathbf{R}_{(l-1)\times(l-1)}^{-1}\mathbf{X}_{l-1}\mathbf{x}(l).$$

IV. Real Image Experiments

Two real image scenes were used for experiments. One is an airborne real image scene collected by Hyperspectral Digital Imagery Collection Experiments (HYDICE), and the other is a spaceborne satellite data, Hyperion image scene.

A. HYDICE Data

The image scene to be studied for experiments is an image scene shown in Fig. 1(a), which has a size of 64 × 64 pixel

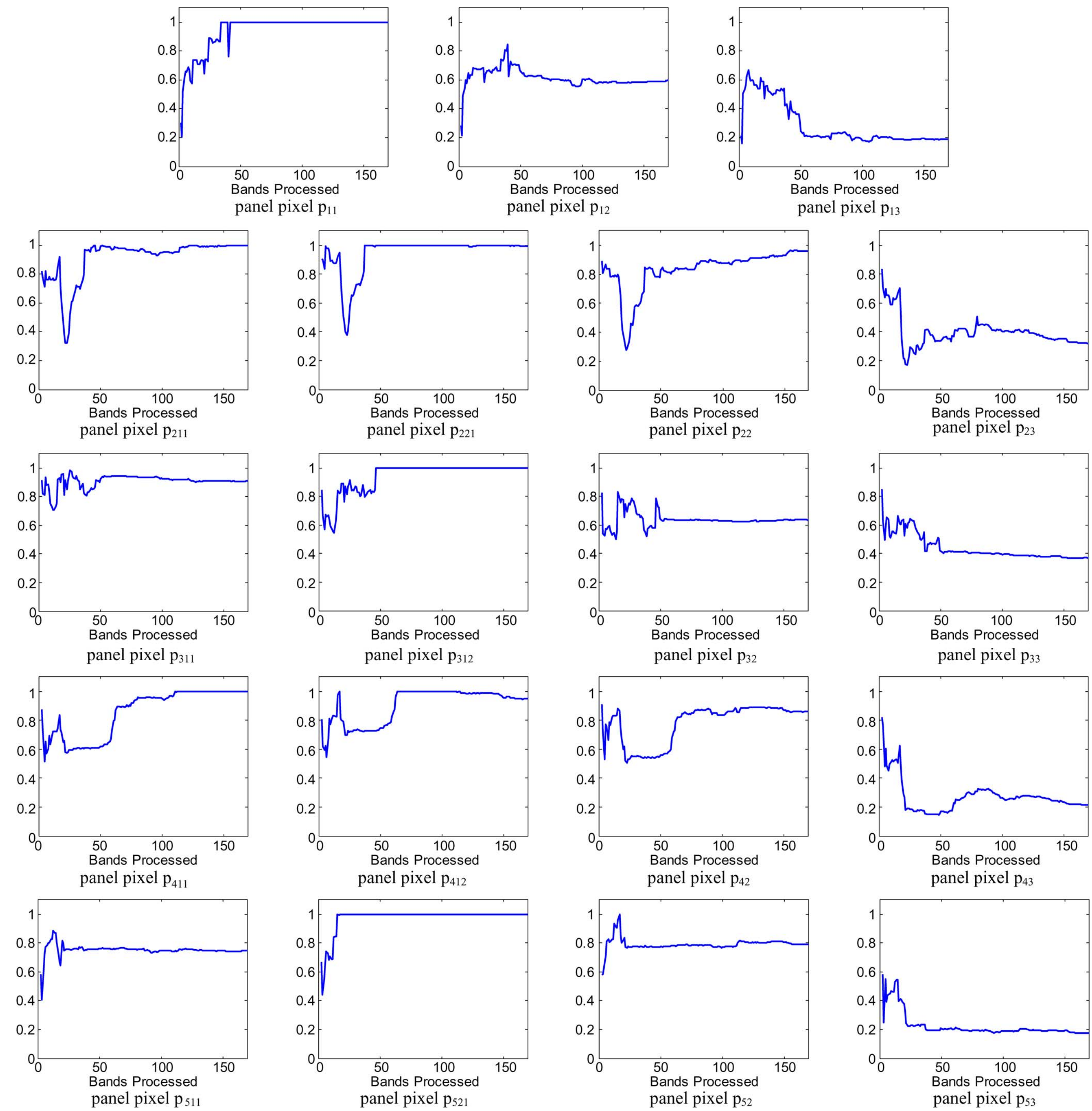

Fig. 2. Relative abundance of 19 red panel pixels in Fig. 1(b) specified by the five panel signatures $\mathbf{p}_1$, $\mathbf{p}_2$, $\mathbf{p}_3$, $\mathbf{p}_4$, and $\mathbf{p}_5$ by PBP-CEM.

vectors with 15 panels in the scene and the ground truth map in Fig. 1(b). It was acquired by 210 spectral bands with a spectral coverage from 0.4 to 2.5 μm. Low-signal/high-noise bands (bands 1–3 and bands 202–210) and water vapor absorption bands (bands 101–112 and bands 137–153) were removed. Therefore, a total of 169 bands were used in the experiments. The spatial resolution is 1.56 m, and the spectral resolution is, on average, 10 nm.

Within the scene in Fig. 1(a), there are a large grass field background and a forest on the left edge. Each element in this matrix is a square panel and denoted by p_{ij}, with rows indexed by i and columns indexed by $j = 1, 2, 3$. For each row $i = 1, 2, \ldots, 5$, there are three panels p_{i1}, p_{i2}, and p_{i3}, painted by the same paint but with three different sizes. The sizes of the panels in the first, second, and third columns are 3 m $\times$ 3 m, 2 m $\times$ 3 m, and 1 m $\times$ 3 m, respectively. Since the size of the panels in the third column is 1 m $\times$ 3 m, they cannot be seen visually from Fig. 1(a) due to the fact that its size is less than the 1.56-m pixel resolution. For each column $j = 1, 2, 3$, the five panels, p_{1j}, p_{2j}, p_{3j}, p_{4j}, and p_{5j} have the same size but with five different paints. However, it should be noted that the panels in rows 2 and 3 were made by the same material with two

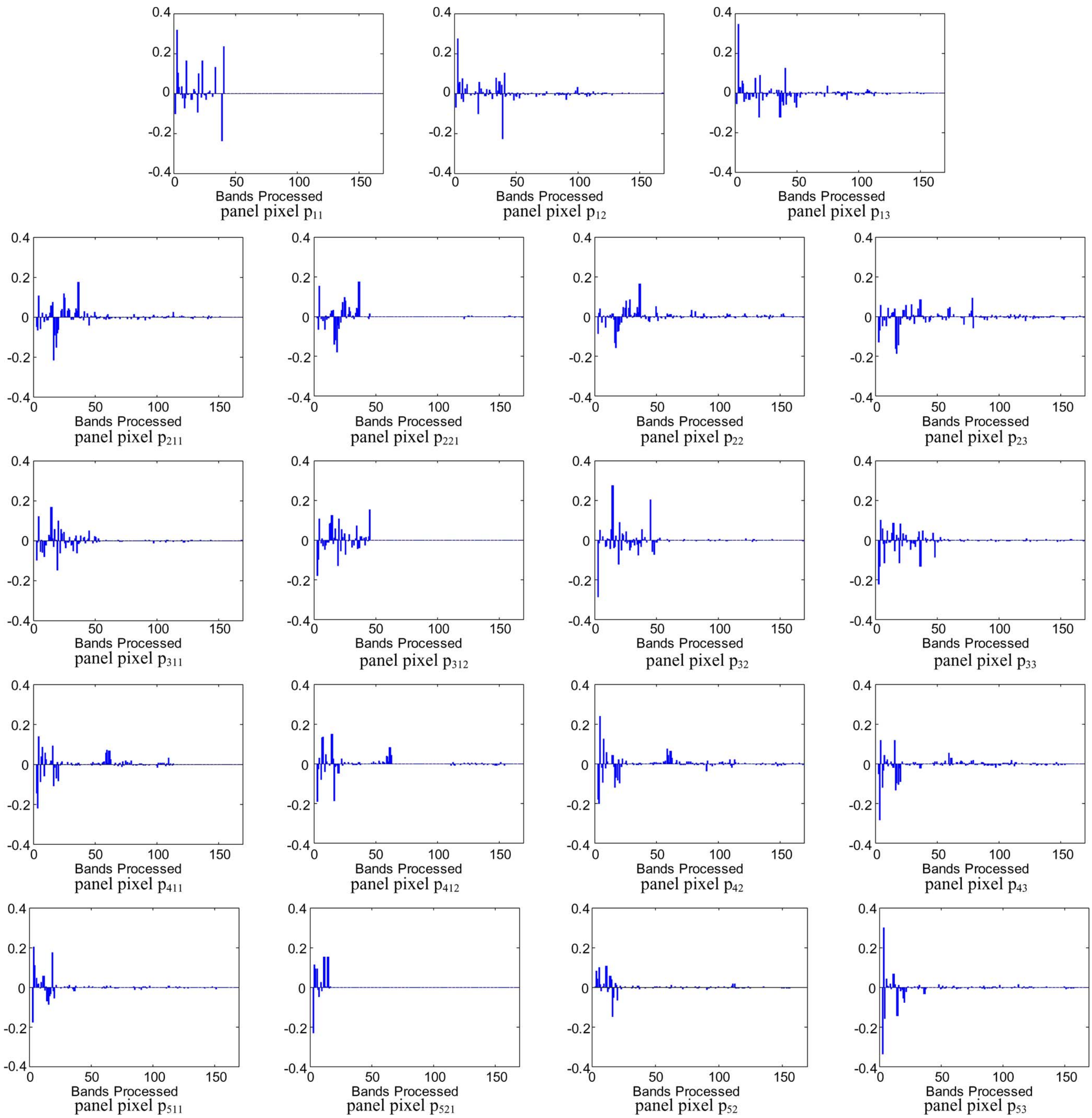

Fig. 3. Difference in relative abundance of the 19 red panel pixels in Fig. 1(b) specified by the five panel signatures $\mathbf{p}_1$, $\mathbf{p}_2$, $\mathbf{p}_3$, $\mathbf{p}_4$, and $\mathbf{p}_5$ between $\delta^{\mathrm{PBP-CEM}}(\mathbf{r}(l))$ and $\delta^{\mathrm{PBP-CEM}}(\mathbf{r}(l-1))$.

different paints. Similarly, it is also the case for panels in rows 4 and 5. Nevertheless, they were still considered as different panels, but our experiments will demonstrate that detecting panels in row 5 (row 4) may also have an effect on detection of panels in row 2 (row 3). The 1.56-m spatial resolution of the image scene suggests that most of the 15 panels are one pixel in size, except for $\mathbf{p}_{21}$, $\mathbf{p}_{31}$, $\mathbf{p}_{41}$, and $\mathbf{p}_{51}$ which are two-pixel panels, denoted by p_{211}, p_{221}, p_{311}, p_{312}, p_{411}, p_{412}, p_{511}, and p_{521}. Fig. 1(b) shows the precise spatial locations of these 15 panels, where red pixels (R pixels) are the panel center pixels and the pixels in yellow (Y pixels) are panel pixels mixed with the background. Fig. 1(c) plots the five panel spectral signatures $\mathbf{p}_i$ for $i = 1, 2, \ldots, 5$ obtained by averaging R pixels in the 3 m × 3 m, 2 m × 2 m, and 1 m × 1 m panels in row i in Fig. 1(b).

It should be noted the R pixels in the 1 m × 1 m panels are not shown in Fig. 1(a) because they are not pure pixels, mainly due to that fact that the spatial resolution of the R pixels in the 1 m × 1 m panels is 1 m, which is smaller than the pixel resolution of 1.56 m in which case the size of the R panel within a single pixel size is approximately $(1.56)^{-2}\,\mathrm{m} \approx 0.4\,\mathrm{m}$. These five panel signatures in Fig. 1(c) were used as required prior target knowledge for the desired target signatures by CEM.

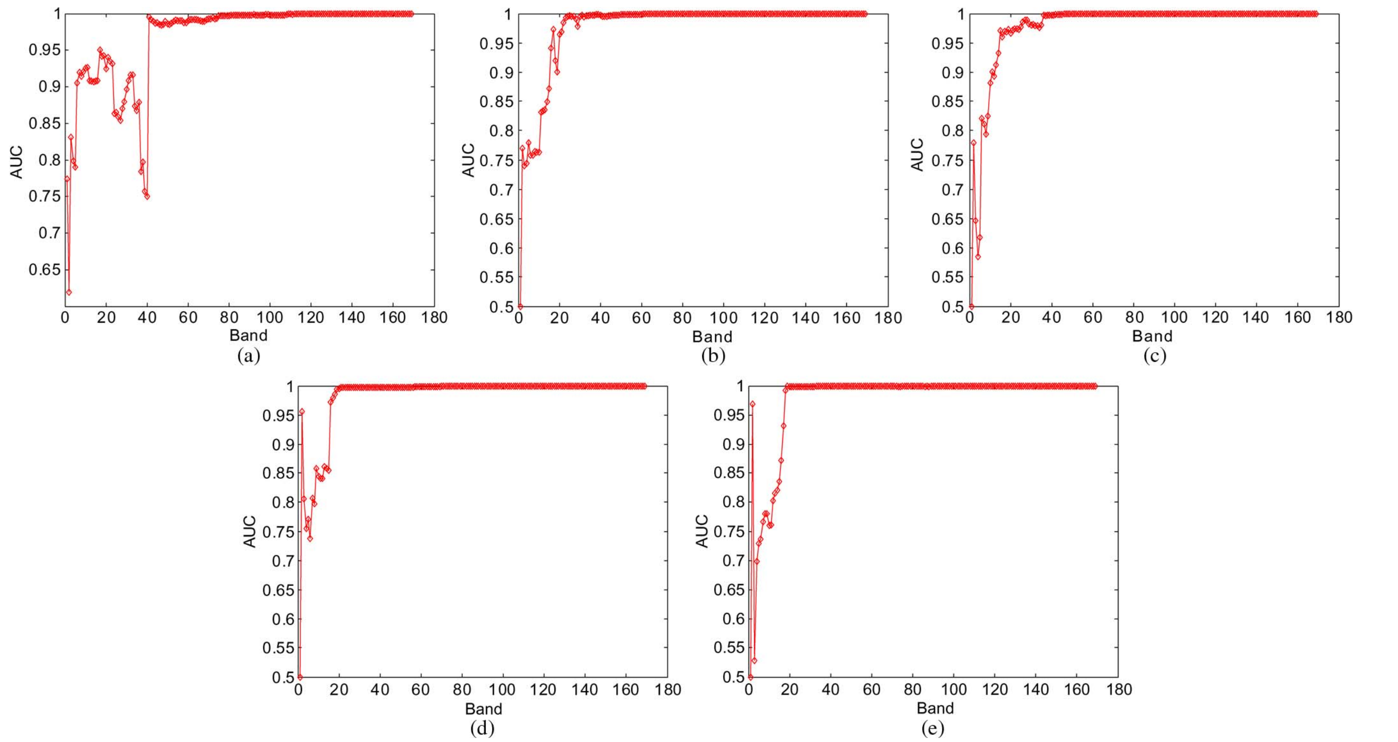

Fig. 4. ROC curves of (band, AUC) for progressive detection performance of PBP-CEM. (a) ROC curve of (band, AUC) for p_{11}, p_{12}, and p_{13}. (b) ROC curve of (band, AUC) for p_{211}, p_{221}, p_{22}, and p_{23}. (c) ROC curve of (band, AUC) for p_{311}, p_{312}, p_{32}, and p_{33}. (d) ROC curve of (band, AUC) for p_{411}, p_{412}, p_{42}, and p_{43}. (e) ROC curve of (band, AUC) for p_{511}, p_{521}, p_{52}, and p_{53}.

Fig. 2(a)–(e) shows the PBP-CEM detected amounts of the 19 R panel pixels p_{11}, p_{12}, p_{13}, p_{211}, p_{221}, p_{22}, p_{23}, p_{311}, p_{312}, p_{32}, p_{33}, p_{411}, p_{412}, p_{42}, p_{43}, p_{511}, p_{521}, p_{52}, and p_{53} with the desired spectral signature $\mathbf{d}$ specified by one of the five panel signatures $\mathbf{p}_1$, $\mathbf{p}_2$, $\mathbf{p}_3$, $\mathbf{p}_4$, and $\mathbf{p}_5$, respectively, as band number is progressively increased from 1 to 169. The y-axis is the detected amount, and the x-axis is the number of bands used to perform PBP-CEM. The displayed detected amounts correspond to the $\delta^{\mathrm{PBP-CEM}}(\mathbf{r}(l))$ for the specified panel pixels. Each value was normalized so that the minimum value is zero and the maximum value is one. Thus, the pixel with the strongest response to the algorithm will have the value of one. Such $\delta^{\mathrm{PBP-CEM}}(\mathbf{r}(l))$-generated abundance fractional amounts are referred to as relative abundance values.

According to Fig. 2, it is clearly shown that over 75% of all 19 R panel pixels located in the first two columns required less than 50 bands to reach similar abundance fractions with little changes detected by CEM using additional new bands beyond 50. Of particular interest are panel pixels p_{411}, p_{412}, and p_{511}, p_{521}, where p_{411} and p_{412} needed more than 50 bands to reach values consistent with CEM while p_{511} and p_{521} required less than half of 50 bands. To further demonstrate differential detected amounts by two consecutive band numbers, Fig. 3(a)–(e) shows the difference in detected abundance fractions of the 19 R panel pixels with the desired signature $\mathbf{d}$ specified by one of the five panel signatures $\mathbf{p}_1$, $\mathbf{p}_2$, $\mathbf{p}_3$, $\mathbf{p}_4$, and $\mathbf{p}_5$ as the band number l is increased from 1 to 169. This can be written mathematically as the difference between detected abundance fractions by $\delta^{\mathrm{PBP-CEM}}(\mathbf{r}(l))$ and $\delta^{\mathrm{PBP-CEM}}(\mathbf{r}(l))$, i.e., $\delta^{\mathrm{PBP-CEM}}(\mathbf{r}(l)) - \delta^{\mathrm{PBP-CEM}}(\mathbf{r}(l-1))$, where the detected amounts were the newly added detected abundance fractions provided by the lth band, $\mathbf{B}_l$ minus the detected amounts from the previous $(l-1)$ bands. This updates the results from the first $(l-1)$ bands $\{\mathbf{B}_j\}_{j=1}^{l-1}$ to the first l bands, $\{\mathbf{B}_j\}_{j=1}^{l}$.

The plots in Fig. 3 provide a better picture of dynamic changes in detected amounts of the 19 R panel pixels as band number is progressively processed. In particular, these plots can be also used to observe fluctuation and saturation in detected amounts which showed that there was no need of using the complete set of bands to perform CEM. As a matter of fact, it could be easily done less than 1/3 of the total number of bands, 169 bands.

Since we have ground truth of the 19 R panel pixels, we can further calculate their detection rates via a receiver operating characteristic (ROC) analysis for performance evaluation [20], i.e., detection of panel pixels p_{11}, p_{12}, and p_{13} using $\mathbf{p}_1$; detection of panel pixels p_{211}, p_{221}, p_{22}, and p_{23} using panel signature $\mathbf{p}_2$; detection of panel pixels p_{311}, p_{312}, p_{32}, and p_{33} using panel signature $\mathbf{p}_3$; detection of panel pixels p_{411}, p_{412}, p_{42}, and p_{43} using panel signature $\mathbf{p}_4$; and detection of panel pixels p_{511}, p_{521}, p_{52}, and p_{53} using panel signature $\mathbf{p}_5$. In order to include the band number as a parameter to see the progressive detection performance of PBP-CEM on these 19 R panel pixels band by band, we do not follow the traditional approach in plotting an ROC curve of detection probability P_{D} versus false alarm probability P_{F}. Instead, we choose the common practice used in medical diagnosis to calculate the area under an ROC curve, referred to as area under curve (AUC) in [21]–[23]. Using such an AUC, an alternative ROC curve can be plotted in terms of AUC in the y-axis versus band number

Fig. 5. (a) Cropped Hyperion image scene EO1H0150322011201110K3. (b) Cropped Hyperion image scene EO1H0150322011201110K3 with five AOIs: beach (dark blue), Westinghouse Bay (green), Mezick Ponds (orange), farm land (light blue), and a corporate building (magenta). (c) Average spectral signatures for each of the five AOIs.

in the x-axis. Fig. 4 plots five ROC curves of (band, AUC) for progressive performance of PBP-CEM in detection of the 19 R panel pixels using five panel signatures in Fig. 1(c) as desired target signatures where $\{\mathbf{B}_j\}_{j=1}^{l}$ are progressively included in the process of (8) with l increased from 1 to 169.

According to Fig. 4, at least 50 bands are required to achieve reasonably well in detecting panel pixels in row 1. However, it only required 40 bands to detect all other R panel pixels in rows 2–5 with AUC nearly close to one. Nevertheless, Fig. 4 demonstrated a fact that, in order for CEM to be effective, there is no need of using full bands. As a matter of fact, only less than 1/3 bands are sufficiently enough to have CEM performed well. In addition, the plots in Fig. 4 also provided information of how a band affects CEM detection performance. This is particularly interesting from Fig. 4(a), where the progressive detection was ups and downs between 8 and 50. Such valuable information will not be offered by any detection technique using full bands to process the data.

B. Hyperion Data

The data to be studied were collected by the Hyperion sensor mounted on the Earth Observer 1 (EO-1) satellite. Hyperion uses a high-resolution hyperspectral imager to record Earth surface images of approximately 7.5 km by 100 km with a 30-m spatial resolution and a 10-nm spectral resolution. The image scene EO1H0150322011201110K3 was downloaded from the USGS Earth Explorer website [24]. The image used is a Hyperion L1 data product which includes 198 channels of calibrated spectral information. This image was then cropped to select a region of interest covering the western side of the Chesapeake Bay Bridge. The resulting image cube is a square with a spatial dimension of size 64×64 and 198 spectral bands ranging from 426 to 2396 nm. The image was then compared with higher resolution areal imagery to identify five distinct areas of interest (AOIs). The areas include a beach, Westinghouse Bay, Mezick Ponds, farm land, and a large corporate building. Four pixels were selected at random from each of these areas and used to generate an average spectral signature for the material contained in the area, with the exception of the farmland which used seven pixels due to the fact that it is composed of four disjoint regions in the image where four pixels were selected from the largest farmland region and a single pixel was chosen from the remaining three regions. A color image of the region and the spectral signatures of each of the five AOIs are shown in Fig. 5.

Using the spectral signatures of five AOIs plotted in Fig. 5(c) as the desired target signatures for CEM, Fig. 6(a)–(e) shows the detected amounts of five AOIs, namely, beach, Westinghouse Bay, Mezick Ponds, farm land, and corporate building, by PBP-CEM, respectively, as band number is progressively increased from 1 to 198, where the y-axis is the detected amount and the x-axis is the number of bands used to perform CEM. Each of these images includes the response due to a randomly selected pixel from within each of the five AOIs. While the pixels were selected randomly, they were compared to the locations chosen for the desired spectral signatures to match what they represented. The pixels used to generate the desired spectral signatures were excluded, with the exception of the corporate building which only consisted of the four pixels used to generate the spectral signature. This allows a comparison of the response for each region relative to each of the five corresponding signatures. Unlike the HYDICE data, there is no complete ground truth about specific targets other than the AOI selected. In addition, the purity of the used desired signatures $\mathbf{d}$ was smeared by the 30-m spatial resolution so that the CEM-detected abundance fractions fluctuated. Nevertheless, analogous to HYDICE experiments, the plots in Fig. 6 also indicated that there was no need of using the complete set of bands, and in most cases, less than 50 bands were required for CEM to perform.

Since the plots in Fig. 6 did not illustrate how progressive detection is performed by CEM in a progressive manner, Fig. 7(a)–(g) visually shows the progression in the detected amounts of abundance for the entire image using the Westinghouse Bay spectral signature for the desired signature $\mathbf{d}$ as the number of band processes was increased. Similar results are also obtained for each spectral signature, with the exception of the Mezick Ponds signature which resulted in poor discrimination; however, they are not included here. It is worth noting that

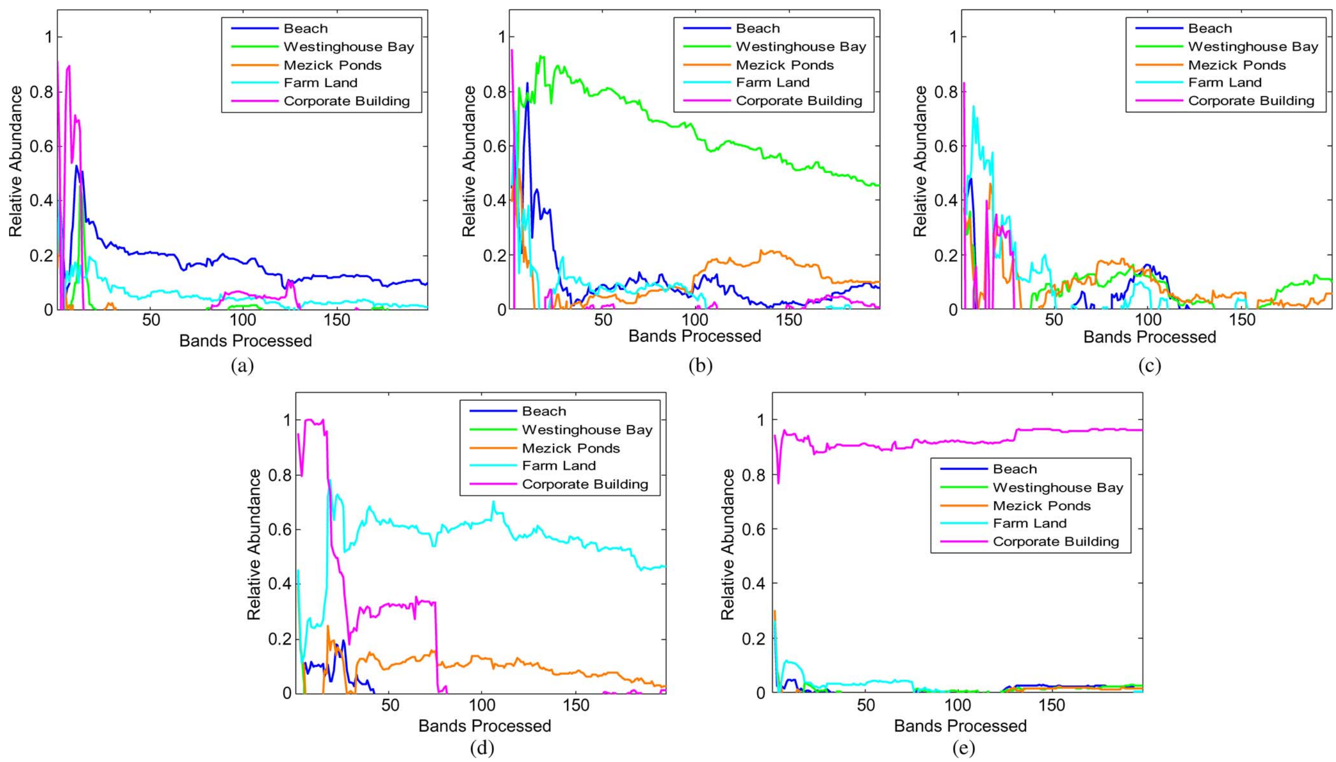

Fig. 6. Relative abundance of five AOIs, namely, beach, Westinghouse Bay, Mezick Ponds, farm land, and corporate building, by PBP-CEM with desired material signatures. (a) $\mathbf{d}$ = beach signature. (b) $\mathbf{d}$ = Westinghouse Bay signature. (c) $\mathbf{d}$ = Mezick Ponds signature. (d) $\mathbf{d}$ = Farm Land signature. (e) $\mathbf{d}$ = Corporate Building.

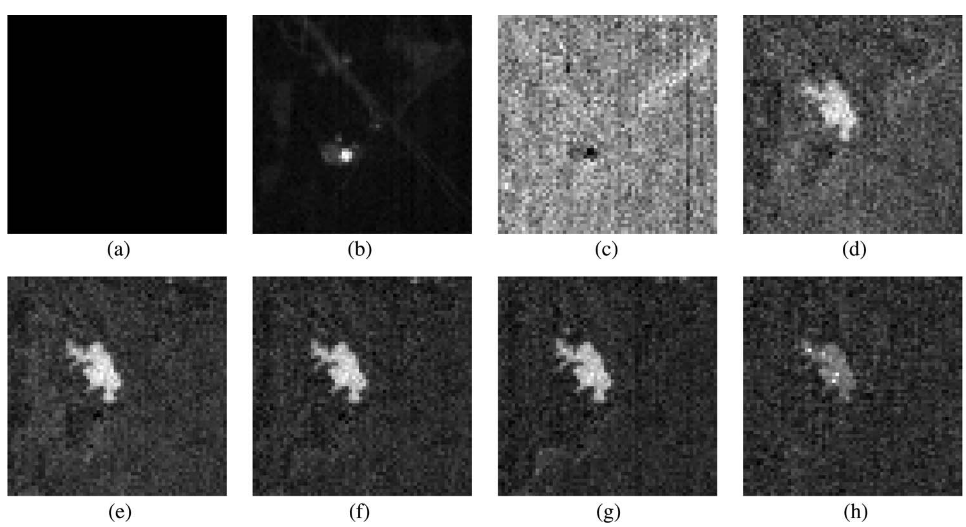

Fig. 7. Result of PBP-CEM using the Westinghouse Bay signature after receiving: (a) 1 band. (b) 2 bands. (c) 10 bands. (d) 20 bands. (e) 30 bands. (f) 40 bands. (g) 60 bands. (h) All bands.

plots similar to Fig. 3 were not applicable due to lack of specific ground truth in the AOIs.

Interestingly, as shown in Fig. 7, after 20 bands, CEM was able to outline the bay area in Fig. 7(d) and to improve the detection results up to 40 bands in Fig. 7(e)–(g), and then, its silhouette began to gradually deteriorate until full bands were used in Fig. 7(h). This experiment further demonstrates that PBP-CEM offers unique advantages of how a detected target varies its detected abundance amount in a progressive manner. Since there is no ground truth provided by this Hyperion data, we are not able to perform ROC analysis for quantitative study.

C. Computational Times

The computational time of PBP-CEM was compared to that of CEM. Each algorithm was run and executed in MATLAB R2012A with an Intel Core i7-3770 running at 3.4 GHz with

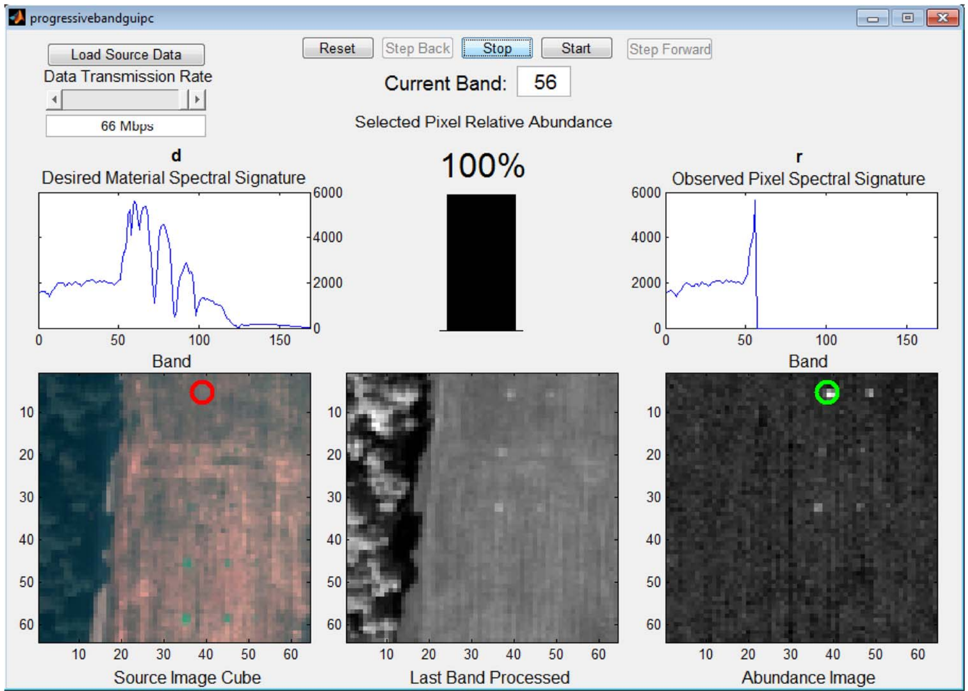

Fig. 8. Snapshot of the developed GUI software.

16 GB of RAM on the HYDICE image five times to produce an average computing time. While CEM required 34.3 ms to complete processing, PBP-CEM required 106.9 ms to complete processing of the first band and 380.2 ms to complete processing of all bands. This is mainly due to the fact that CEM only calculates the global sample correlation matrix $\mathbf{R}$ prior to its processing, and once it is done, it does not have to do it again. By contrast, PBP-CEM must recalculate the sample-varying correlation matrix via a recursive equation specified by (8). Of course, PBP-CEM requires more time for data processing than CEM does. However, such disadvantage can be offset by several benefits. One is progressive detection performance as bands are progressively processed. Second, with such progressive performance, we can learn the impact of each band on CEM performance. Third, the recursive equation (12) provides feasible implementation of hardware design. Finally, PBP-CEM can begin as soon as the first band has been received as opposed to CEM which must wait for data to be completed before it can calculate the matrix $\mathbf{R}$.

V. GUI

A graphical user interface (GUI) with a screenshot shown in Fig. 8 was developed using MATLAB's *guide* to aid in algorithm performance analysis. The GUI allows the user to load different data sources for analysis. At the bottom of the GUI, there are three image display windows. The images displayed from left to right are a color image of the scene, a grayscale image of the last band processed, and the current abundance image. Once the data are loaded, the user is given an option to select a pixel from the image to be the target material $\mathbf{d}$. Once the desired pixel is selected, the user can start processing by clicking the start button. The program then simulates data transmission by using the MATLAB timer function. At each timer tick, one complete band of data is considered received, and PBP-CEM processes the newly received data. Upon completion of processing, the abundance image and the last band processed images are updated to allow the user to observe the results. A text box indicating the current band is displayed at the top center so that the user can easily tell how many bands have been processed. The cycle repeats until all bands have been processed or the user clicks on the stop button. If the processing is stopped, it may be continued from the current band or reset to begin processing at the first band. The user may adjust the simulated transmission rate by adjusting a slide bar in the upper left-hand corner of the GUI. The range of data rates varies from 66 kb/s to 66 Mb/s and assumes that the data consist of 16-b numbers. The user is also given an opportunity to observe the spectral signatures of both the desired material and any pixel in the abundance image. The two spectral signatures are located above their corresponding images. Their corresponding pixels are highlighted by a red circle for the desired material $\mathbf{d}$ and green for the observed pixel $\mathbf{r}$. In the case of the desired material spectral signature, the complete signature is displayed. In the case of the observed pixel spectral signature, only the bands that have been received and processed are displayed. Finally, the relative abundance for the observed pixel is displayed in the center of the GUI.

According to Fig. 8, the developed GUI processes PBP-CEM whenever new bands are added. The processing can be carried out band by band in a real-time fashion.

VI. Conclusion

This paper has presented a new look of CEM, called PBP-CEM, in its applications in satellite data processing. It makes use of CBCM to adapt CEM to different bands. Since CBCM varies with bands, a recursive innovations information update equation is specifically derived to avoid repeatedly recalculating CBCM, where only the information provided by a new incoming band is needed to be processed for updating results. As a result, PBP-CEM can be made to perform as if it is a real-time processing algorithm in the sense of data transmission and communication when ground stations receive data information from different bands sequentially. In this case, PBP-CEM can be performed instantly as the information in the new bands is received. To further materialize its practical value in applications, a GUI software is also developed to allow users to process

$$
\begin{aligned}
\mathbf{R}_{l\times l}^{-1} &= \begin{bmatrix} \mathbf{X}_{l-1}\mathbf{X}_{l-1}^T & \mathbf{X}_{l-1}\mathbf{x}(l) \\ \mathbf{x}^T(l)\mathbf{X}_{l-1}^T & \mathbf{x}^T(l)\mathbf{x}(l) \end{bmatrix}^{-1} \\
&= \begin{bmatrix} \left(\mathbf{X}_{l-1}\mathbf{X}_{l-1}^T\right)^{-1} + \beta\left(\mathbf{X}_{l-1}\mathbf{X}_{l-1}^T\right)^{-1}\mathbf{X}_{l-1}\mathbf{x}(l)\mathbf{x}^T(l)\left[\left(\mathbf{X}_{l-1}\mathbf{X}_{l-1}^T\right)^{-1}\mathbf{X}_{l-1}\right]^T & -\beta\left(\mathbf{X}_{l-1}\mathbf{X}_{l-1}^T\right)^{-1}\mathbf{X}_{l-1}\mathbf{x}(l) \\ -\beta\mathbf{x}^T(l)\left[\left(\mathbf{X}_{l-1}\mathbf{X}_{l-1}^T\right)^{-1}\mathbf{X}_{l-1}^T\right]^T & \beta \end{bmatrix} \\
&= \begin{bmatrix} \left(\mathbf{X}_{l-1}\mathbf{X}_{l-1}^T\right)^{-1} + \beta\left(\mathbf{X}_{l-1}\mathbf{X}_{l-1}^T\right)^{-1}\mathbf{X}_{l-1}\mathbf{x}(l)\mathbf{x}^T(l)\left[\left(\mathbf{X}_{l-1}\mathbf{X}_{l-1}^T\right)^{-1}\mathbf{X}_{l-1}\right]^T & -\dfrac{\left(\mathbf{X}_{l-1}\mathbf{X}_{l-1}^T\right)^{-1}\mathbf{X}_{l-1}\mathbf{x}(l)}{\left(\mathbf{x}^T(l)P_{\mathbf{X}_{l-1}^T}^{\perp}\mathbf{x}(l)\right)} \\ -\dfrac{\mathbf{x}^T(l)\left[\left(\mathbf{X}_{l-1}\mathbf{X}_{l-1}^T\right)^{-1}\mathbf{X}_{l-1}\right]^T}{\left(\mathbf{x}^T(l)P_{\mathbf{X}_{l-1}^T}^{\perp}\mathbf{x}(l)\right)} & \left(\mathbf{x}^T(l)P_{\mathbf{X}_{l-1}^T}^{\perp}\mathbf{x}(l)\right)^{-1} \end{bmatrix}
\end{aligned}
\tag{A1}
$$

$$
\begin{aligned}
\mathbf{R}_{l\times l}^{-1} &= \left[\left(\frac{1}{N}\right)\mathbf{X}_l\mathbf{X}_l^T\right]^{-1} = N\begin{bmatrix} \mathbf{X}_{l-1}\mathbf{X}_{l-1}^T & \mathbf{X}_{l-1}\mathbf{x}(l) \\ \mathbf{x}^T(l)\mathbf{X}_{l-1}^T & \mathbf{x}^T(l)\mathbf{x}(l) \end{bmatrix}^{-1} \\
&= \begin{bmatrix} \left(\left(\frac{1}{N}\right)\mathbf{X}_{l-1}\mathbf{X}_{l-1}^T\right)^{-1} + \left(\frac{1}{N}\right)\dfrac{\left(\left(\frac{1}{N}\right)\mathbf{X}_{l-1}\mathbf{X}_{l-1}^T\right)^{-1}\mathbf{X}_{l-1}\mathbf{x}(l)\mathbf{x}^T(l)\left[\left(\left(\frac{1}{N}\right)\mathbf{X}_{l-1}\mathbf{X}_{l-1}^T\right)^{-1}\mathbf{X}_{l-1}\right]^T}{\left(\mathbf{x}^T(l)P_{\mathbf{X}_{l-1}^T}^{\perp}\mathbf{x}(l)\right)} & -\dfrac{\left(\left(\frac{1}{N}\right)\mathbf{X}_{l-1}\mathbf{X}_{l-1}^T\right)^{-1}\mathbf{X}_{l-1}\mathbf{x}(l)}{\left(\mathbf{x}^T(l)P_{\mathbf{X}_{l-1}^T}^{\perp}\mathbf{x}(l)\right)} \\ -\dfrac{\mathbf{x}^T(l)\left[\left(\left(\frac{1}{N}\right)\mathbf{X}_{l-1}\mathbf{X}_{l-1}^T\right)^{-1}\mathbf{X}_{l-1}\right]^T}{\left(\mathbf{x}^T(l)P_{\mathbf{X}_{l-1}^T}^{\perp}\mathbf{x}(l)\right)} & N\left(\mathbf{x}^T(l)P_{\mathbf{X}_{l-1}^T}^{\perp}\mathbf{x}(l)\right)^{-1} \end{bmatrix} \\
&= \begin{bmatrix} \mathbf{R}_{(l-1)\times(l-1)}^{-1} + \left(\frac{1}{N}\right)\dfrac{\mathbf{R}_{(l-1)\times(l-1)}^{-1}\mathbf{X}_{l-1}\mathbf{x}(l)\left[\mathbf{R}_{(l-1)\times(l-1)}^{-1}\mathbf{X}_{l-1}\mathbf{x}(l)\right]^T}{\left(\mathbf{x}^T(l)P_{\mathbf{X}_{l-1}^T}^{\perp}\mathbf{x}(l)\right)} & -\dfrac{\mathbf{R}_{(l-1)\times(l-1)}^{-1}\mathbf{X}_{l-1}\mathbf{x}(l)}{\left(\mathbf{x}^T(l)P_{\mathbf{X}_{l-1}^T}^{\perp}\mathbf{x}(l)\right)} \\ -\dfrac{\left[\mathbf{R}_{(l-1)\times(l-1)}^{-1}\mathbf{X}_{l-1}\mathbf{x}(l)\right]^T}{\left(\mathbf{x}^T(l)P_{\mathbf{X}_{l-1}^T}^{\perp}\mathbf{x}(l)\right)} & N\left(\mathbf{x}^T(l)P_{\mathbf{X}_{l-1}^T}^{\perp}\mathbf{x}(l)\right)^{-1} \end{bmatrix}
\end{aligned}
\tag{A2}
$$

$$
\begin{aligned}
&\delta^{\mathrm{PBP}-CEM}\left(\mathbf{r}(l)\right) \\
&= \kappa_l\mathbf{d}^T(l)(\mathbf{R}_{l\times l})^{-1}\mathbf{r}(l) \\
&= \kappa_l\left(\mathbf{d}(l-1), d_l\right)^T \\
&\quad \begin{bmatrix} \left(\mathbf{R}_{(l-1)(l-1)}^T\right)^{-1} + \left(\frac{1}{N}\right)\beta_{l|(l-1)}\mathbf{R}_{(l-1)\times(l-1)}^{-1}\mathbf{X}_{l-1}\mathbf{x}(l)\left(\mathbf{R}_{(l-1)\times(l-1)}^{-1}\mathbf{X}_{l-1}\mathbf{x}(l)\right)^T & -\beta_{l|(l-1)}\mathbf{R}_{(l-1)\times(l-1)}^{-1}\mathbf{X}_{l-1}\mathbf{x}(l) \\ -\beta_{l|(l-1)}\mathbf{x}(l)\left(\mathbf{R}_{(l-1)\times(l-1)}^{-1}\mathbf{X}_{l-1}\mathbf{x}(l)\right)^T & N\beta_{l|(l-1)} \end{bmatrix} \\
&\quad \times \begin{pmatrix} \mathbf{r}(l-1) \\ r_l \end{pmatrix} \\
&= \kappa_l\mathbf{d}^T(l-1)\left(\mathbf{R}_{(l-1)\times(l-1)}\right)^{-1}\mathbf{r}(l-1) + \left(\frac{1}{N}\right)\kappa_l\beta_{l|(l-1)}\mathbf{d}^T(l-1)\boldsymbol{\nu}_{l|(l-1)}\boldsymbol{\nu}_{l|(l-1)}^T\mathbf{r}(l-1) \\
&\quad - \kappa_l d_l\beta_{l|(l-1)}\boldsymbol{\nu}_{l|(l-1)}^T\mathbf{r}(l-1) - \kappa_l\beta_{l|(l-1)}\mathbf{d}^T(l-1)\boldsymbol{\nu}_{l|(l-1)}r_l + N\kappa_l d_l\beta_{l|(l-1)}r_l \\
&= \left(\frac{\kappa_l}{\kappa_{l-1}}\right)\delta^{\mathrm{PBP-CEM}}\left(\mathbf{r}(l-1)\right) + \left(\frac{1}{N}\right)\kappa_l\beta_{l|(l-1)}\left(\mathbf{d}^T(l-1)\boldsymbol{\nu}_{l|(l-1)} - Nd_l\right)\left(\boldsymbol{\nu}_{l|(l-1)}^T\mathbf{r}(l-1) - Nr_l\right)
\end{aligned}
\tag{A3}
$$

$$
\begin{aligned}
\kappa_l &= \mathbf{d}^T(l)(\mathbf{R}_{l\times l})^{-1}\mathbf{d}(l) \\
&= (\mathbf{d}(l-1), d_l)^T \\
&\quad \times \begin{bmatrix} \left(\mathbf{R}^T_{(l-1)(l-1)}\right)^{-1} + \left(\frac{1}{N}\right)\beta_{l|(l-1)}\mathbf{R}^{-1}_{(l-1)\times(l-1)}\mathbf{X}_{l-1}\mathbf{x}(l)\mathbf{x}^T(l)\left(\mathbf{R}^{-1}_{(l-1)\times(l-1)}\mathbf{X}_{l-1}\right)^T & -\beta_{l|(l-1)}\mathbf{R}^{-1}_{(l-1)\times(l-1)}\mathbf{X}_{l-1}\mathbf{x}(l) \\ -\beta_{l|(l-1)}\mathbf{x}^T(l)\left(\mathbf{R}^{-1}_{(l-1)\times(l-1)}\mathbf{X}_{l-1}\right)^T & N\beta_{l|(l-1)} \end{bmatrix} \\
&\quad \times \begin{pmatrix} \mathbf{d}(l-1) \\ d_l \end{pmatrix} \\
&= \mathbf{d}^T(l-1)\left(\mathbf{R}_{(l-1)\times(l-1)}\right)^{-1}\mathbf{d}(l-1) + \left(\frac{1}{N}\right)\beta_{l|(l-1)}\mathbf{d}^T(l-1)\boldsymbol{\nu}_{l|(l-1)}\boldsymbol{\nu}^T_{l|(l-1)}\mathbf{d}(l-1) \\
&\quad - d_l\beta_{l|(l-1)}\boldsymbol{\nu}^T_{l|(l-1)}\mathbf{d}(l-1) - \beta_{l|(l-1)}\mathbf{d}^T(l-1)\boldsymbol{\nu}_{l|(l-1)}d_l + Nd_l\beta_{l|(l-1)}d_l \\
&= \kappa_{l-1} + \left(\frac{1}{N}\right)\beta_{l|(l-1)}\left(\mathbf{d}^T(l-1)\boldsymbol{\nu}_{l|(l-1)} - Nd_l\right)^2
\end{aligned} \tag{A4}
$$

CEM band by band progressively in real time according to BSQ format.

APPENDIX

In this appendix, we derive a recursive equation to calculate the inverse of the causal sample correlation matrix $\mathbf{R}^{-1}_{l\times l}$ band by band via $\mathbf{R}^{-1}_{(l-1)\times(l-1)}$ progressively while band processing is ongoing and bands being collected in real time and causality (see (A1), shown on the previous page), which leads to (A2) (shown on the previous page). Using (A2), the PBP-CEM subpixel detector, $\delta^{\text{PBP-CEM}}(\mathbf{r}(l))$, can be derived by (A3) (shown at the bottom of the previous page), where $\kappa_l = (\mathbf{d}^T(l)\mathbf{R}^{-1}_{l\times l}\mathbf{d}(l))^{-1}$ is a scalar, $\mathbf{v}_{l|(l-1)} = \mathbf{R}^{-1}_{(l-1)\times(l-1)}\mathbf{X}_{l-1}\mathbf{x}(l)$, and $\beta_{l|(l-1)} = \{\mathbf{x}^T(l)[P^{\perp}_{\mathbf{X}^T_{l-1}}]\mathbf{x}(l)\}^{-1}$. See also (A4), shown at the top of the page, where κ_l can be calculated by updating κ_{l-1}. Of course, κ_l in (A4) can be calculated directly by $\kappa_l(\mathbf{d}^T(l)\mathbf{R}^{-1}_{l\times l}\mathbf{d}(l))^{-1}$ since $\mathbf{d}$ is known *a priori*.

REFERENCES

[1] C.-I. Chang, *Hyperspectral Imaging: Techniques for Spectral Detection and Classification*. Dordrecht, The Netherlands: Kluwer, 2003.

[2] R. B. Singer and T. B. McCord, "Mars: Large scale mixing of bright and dark surface materials and implications for analysis of spectral reflectance," in *Proc. 10th Lunar Planet. Sci. Conf.*, 1979, pp. 1835–1848.

[3] J. B. Adams and M. O. Smith, "Spectral mixture modeling: A new analysis of rock and soil types at the Viking lander 1 suite," *J. Geophys. Res.*, vol. 91, no. B8, pp. 8098–8112, Jul. 10, 1986.

[4] A. R. Gillespie *et al.*, "Interpretation of residual images: Spectral mixture analysis of AVIRIS images, Owens Valley, California," in *Proc. 2nd AVIRIS Workshop*, 1990, pp. 243–270.

[5] J. B. Adams, M. O. Smith, and A. R. Gillespie, "Image spectroscopy: Interpretation based on spectral mixture analysis," in *Remote Geochemical Analysis: Elemental and Mineralogical Composition*, C. M. Pieters and P. A. Englert, Eds. Cambridge, U.K.: Cambridge Univ. Press, 1993, pp. 145–166.

[6] M. O. Smith, J. B. Adams, and D. E. Sabol, "Spectral mixture analysis-new strategies for the analysis of multispectral data," in *Image Spectroscopy—A Tool for Environmental Observations*, J. Hill and J. Mergier, Eds. Dordrecht, The Netherlands: Springer-Verlag, 1994, pp. 125–143, ECSC, EEC, EAEC, Brussels and Luxembourg.

[7] A. Robin, L. Moisan, and S. Le Hegarat-Mascle, "An a-contrario approach for subpixel change detection in satellite imagery," *IEEE Trans. Pattern Anal. Mach. Intell.*, vol. 32, no. 11, pp. 1977–1993, Nov. 2010.

[8] J. C. Harsanyi, W. Farrand, J. Hejl, and C.-I. Chang, "Automatic identification of spectral endmembers in hyperspectral image sequences," in *Proc. ISSSR*, San Diego, CA, USA, Jul. 10–15, 1994, pp. 267–277.

[9] J. C. Harsanyi, "Detection and Classification of Subpixel Spectral Signatures in Hyperspectral Image Sequences," Ph.D. dissertation, Dept. Elect. Eng., Univ. Maryland Baltimore County, Baltimore, MD, USA, Aug. 1993.

[10] R. S. Resmini, M. E. Kappus, W. S. Aldrich, J. C. Harsanyi, and M. Anderson, "Mineral mapping with Hyperspectral Digital Imagery Collection Experiment (HYDICE) sensor data at Cuprite, Nevada, U.S.A.," *Int. J. Remote Sens.*, vol. 18, no. 17, pp. 1553–1570, May 1997.

[11] C.-I. Chang, "Target signature-constrained mixed pixel classification for hyperspectral imagery," *IEEE Trans. Geosci. Remote Sens.*, vol. 40, no. 3, pp. 1065–1081, May 2002.

[12] C.-I. Chang, "Orthogonal subspace projection revisited: A comprehensive study and analysis," *IEEE Trans. Geosci. Remote Sens.*, vol. 43, no. 3, pp. 502–518, Mar. 2005.

[13] Y. Wang, R. Schultz, S. Y. Chen, C. Liu, and C.-I. Chang, "Progressive constrained energy minimization for subpxiel detection," in *Proc. SPIE Conf. Algorithms Technol. Multispectr., Hyperspectr. Ultraspectr. Imagery XIX*, Baltimore, MD, USA, 29 Apr.–3 May 2013, pp. 874321-1–874321-7.

[14] R. A. Schowengerdt, *Remote Sensing: Models and Methods for Image Processing*., 2nd ed. San Diego, CA, USA: Academic, 1997.

[15] C.-I. Chang, S. Wang, K. H. Liu, and C. Lin, "Progressive band dimensionality expansion and reduction for hyperspectral imagery," *IEEE J. Sel. Topics Appl. Earth Observ. Remote Sens.*, vol. 4, no. 3, pp. 591–614, Sep. 2011.

[16] C.-I. Chang, *Hyperspectral Data Processing: Algorithm Design and Analysis*. Hoboken, NJ, USA: Wiley, 2013.

[17] H. Poor, *An Introduction to Signal Detection and Estimation*. New York, NY, USA: Springer-Verlag, 1991.

[18] O. L. Frost, III, "An algorithm for linearly constrained adaptive array processing," *Proc. IEEE*, vol. 60, no. 8, pp. 926–935, Aug. 1972.

[19] J. J. Settle, "On the relationship between spectral unmixing and subspace projection," *IEEE Trans. Geosci. Remote Sens.*, vol. 34, no. 4, pp. 1045–1046, Jul. 1996.

[20] H. V. Poor, *An Introduction to Signal Detection and Estimation*. New York, NY, USA: Springer-Verlag, 1994.

[21] C.-I. Chang, X. Zhao, M. L. G. Althouse, and J.-J. Pan, "Least squares subspace projection approach to mixed pixel classification in hyperspectral images," *IEEE Trans. Geosci. Remote Sens.*, vol. 36, no. 3, pp. 898–912, May 1998.

[22] J. A. Swets and R. M. Pickett, *Evaluation of Diagnostic Systems: Methods From Signal Detection Theory*. New York, NY, USA: Academic, 1982.

[23] C. E. Metz, "ROC methodology in radiological imaging," *Invest. Radiol.*, vol. 21, no. 9, pp. 720–723, Sep. 1986.

[24] EarthExplorer, Sep. 1, 2013. [Online]. Available: http://earthexplorer.usgs.gov/

Chein-I Chang (S'81–M'87–SM'92–F'10) received the B.S. degree in mathematics from Soochow University, Taipei, Taiwan, the M.S. degree in mathematics from the Institute of Mathematics, National Tsing Hua University, Hsinchu, Taiwan, the M.A. degree in mathematics from the State University of New York at Stony Brook, Stony Brook, NY, USA, the M.S. and M.S.E.E. degrees from the University of Illinois at Urbana–Champaign, Urbana, IL, USA, and the Ph.D. degree in electrical engineering from the University of Maryland, College Park, MD, USA.

He has been with the University of Maryland, Baltimore County, Baltimore, MD, USA, since 1987, where he is currently a Professor with the Department of Computer Science and Electrical Engineering. He has also been a Distinguished Chair Professor with National Chung Hsing University, Taichung, Taiwan, since 2014. He was a Visiting Research Specialist with the Institute of Information Engineering, National Cheng Kung University, Tainan, Taiwan, from 1994 to 1995. Additionally, he was a Distinguished Lecturer Chair with National Chung Hsing University, sponsored by the Ministry of Education of Taiwan, from 2005 to 2006. He was a Chair Professor with the Environmental Restoration and Disaster Reduction Research Center and the Department of Electrical Engineering, National Chung Hsing University, where he has been the Chair Professor of remote sensing technology since 2009. He is also currently a Chair Professor with Providence University, Taichung, and an International Chair Professor with National Taipei University of Technology, Taipei. He was a Distinguished Visiting Fellow/Fellow Professor sponsored by the National Science Council in Taiwan from 2009 to 2010. He has five patents and several pending on hyperspectral image processing. He was the Guest Editor of a special issue of the *Journal of High Speed Networks* on *Telemedicine and Applications* in April 2000 and the Coguest Editor of another special issue of the same journal on *Broadband Multimedia Sensor Networks in Healthcare Applications* in April 2007. He is also the Coguest Editor of a special issue on High Performance Computing of Hyperspectral Imaging for the *International Journal of High Performance Computing Applications* in December 2007 and of a special issue on *Signal Processing and System Design in Health Care Applications* for the *EURASIP Journal on Advances in Signal Processing* in 2009. He is currently an Associate Editor of *Artificial Intelligence Research* and also on the editorial boards of *Journal of High Speed Networks*, *Recent Patents on Mechanical Engineering*, *International Journal of Computational Sciences and Engineering*, *Journal of Robotics and Artificial Intelligence*, and *Open Remote Sensing Journal*. He is the author of two books, namely, *Hyperspectral Imaging: Techniques for Spectral Detection and Classification* (Kluwer, 2003) and *Hyperspectral Data Processing: Signal Processing Algorithm Design and Analysis* (Wiley, 2013). He edited two books, namely, *Recent Advances in Hyperspectral Signal and Image Processing* (Transworld Research Network, 2006) and *Hyperspectral Data Exploitation: Theory and Applications* (Wiley, 2007), and co-edited with A. Plaza a book on *High Performance Computing in Remote Sensing* (CRC Press, 2007). He is currently working on a third book, *Real Time Hyperspectral Image Processing: A Progressive Hyperspectral Imaging Perspective* (Springer-Verlag, 2014). His research interests include multispectral/hyperspectral image processing, automatic target recognition, and medical imaging.

Dr. Chang is a Fellow of SPIE. He was an Associate Editor in the area of hyperspectral signal processing for the IEEE TRANSACTIONS ON GEOSCIENCE AND REMOTE SENSING in 2001–2007. He was a plenary speaker for the *Society for Photo-optical Instrumentation Engineers (SPIE)Optics+Applications, Remote Sensing Symposium* in 2009. In addition, he was also a keynote speaker at the *User Conference of Hyperspectral Imaging 2010*, December 30, 2010, Industrial Technology Research Institute, Hsinchu; *2009 Annual Meeting of the Radiological Society of the Republic of China*, 2009, Taichung; *2008 International Symposium on Spectral Sensing Research* in 2008; and *Conference on Computer Vision, Graphics, and Image Processing 2003*, Kimen and 2013, Nan-Tou, Taiwan. He received a National Research Council Senior Research Associateship Award from 2002 to 2003 sponsored by the U.S. Army Soldier and Biological Chemical Command, Edgewood Chemical and Biological Center, Aberdeen Proving Ground, MD.

Robert C. Schultz received the B.S. and M.S. degrees in electrical engineering from Florida Atlantic University, Boca Raton, FL, USA, in 1999 and the Ph.D. degree in electrical engineering from the University of Maryland, Baltimore County, Baltimore, MD, USA, in 2014.

From 2011 to 2014, he was an Assistant Professor with the United States Naval Academy, Annapolis, MD, USA. His research interests include signal processing, communications, and digital electronics.

Marissa C. Hobbs received the B.S. and M.S. degrees in electrical engineering from the University of Texas, San Antonio, TX, USA, in 2002 and 2008, respectively. She is currently working toward the Ph.D. degree in electrical engineering at the University of Maryland, Baltimore County, Baltimore, MD, USA.

From 2012 to 2013, she was a Senior Instructor with the U.S. Naval Academy, Annapolis, MD, USA. Her research interests include signal processing and remote sensing

Shih-Yu Chen received the B.S. degree in electrical engineering from Da-Yeh University, Changhua, Taiwan, in 2005, M.S.E.E. degree from National Chung Hsing University, Taichung, Taiwan, in 2010, and Ph.D. degree in electrical engineering from the University of Maryland, Baltimore County (UMBC), Baltimore, MD, USA, in May 2014.

He is currently an Assistant Professor in Department of Computer Science and Information Engineering, National Yulin University of Science and Technology, Yulin, Taiwan. His research interests include medical images, remote sensing images, and vital sign signal processing.

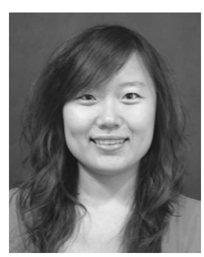

Yulei Wang is currently working toward the Ph.D. degree in the College of Information and Communication Engineering, Harbin Engineering University, Harbin, China.

She was a Visiting Scholar with the Remote Sensing Signal and Image Processing Laboratory, University of Maryland, Baltimore County, Baltimore, MD, USA, awarded by China Scholarship Council in 2011. Her current research interests include hyperspectral image processing and vital sign signal processing.

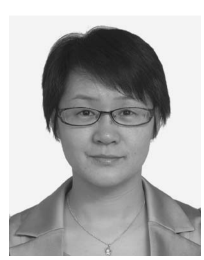

Chunhong Liu received the Ph.D. degree in signal and information processing from Harbin Engineering University, Harbin, China, in 2005.

She is currently an Associate Professor with the Information and Electrical Engineering Department, China Agricultural University, Beijing, China. She has projects currently being supported by China Postdoctoral Science Foundation and National Natural Science Fund of China. She has also conducted more than ten projects in the information and communication field. Her research interests include target detection, transmission, and processing of hyperspectral images.